

Received
Accepted

Supplementary Information For: Real-time Subcellular Imaging Based on Graphene Biosensor

DOI:

www.rsc.org/

Lixun Sun,^{a,#} Yuquan Zhang,^{b,#} Yijia Wang,^c Yong Yang,^{a†} Chonglei Zhang,^b Xiaoyu Weng,^b Siwei Zhu,^c and Xiaocong Yuan^{b†}

Generation of POV Beam

Perfect optical vortex (POV) beam^{1,2} with narrow ring width and controllable beam diameter is simulated and experimentally generated to satisfy the most incident angle for graphene in an optical focusing and differential detection structure. It can be approximately generated through the Fourier transform of a Bessel-Gauss beam in experiments. The programmable spatial light modulator is used to load the phase information of an axicon, a spiral phase plate and a blazed grating. Then the beam is Fourier-transformed through a lens, at whose focal plane it forms the explicit POV beam.

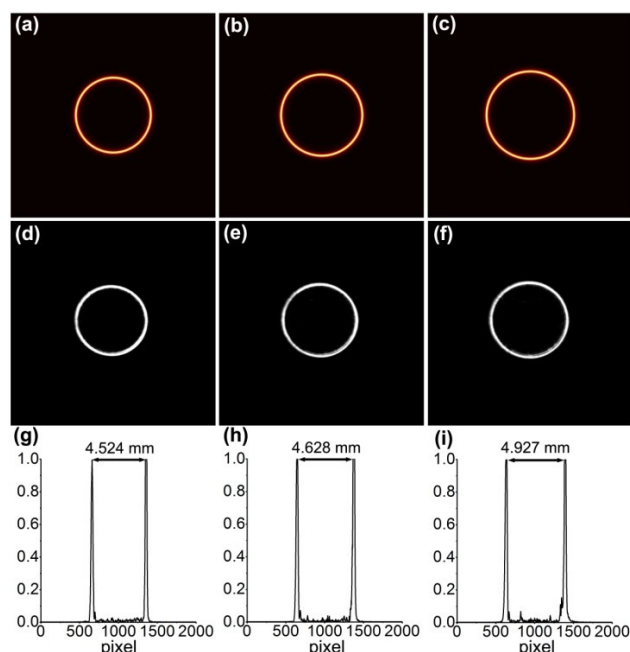


Fig. S1 (a)-(c) Simulated and (d)-(f) experimentally generated ring-shaped POV spots with increasing diameters from left to right. (g)-(i) Intensity profiles across the three generated POV spot centres, the diameter is calculated by counting the 6.5- μm -wide pixel on CCD image.

^a Key Laboratory of Optical Information Science and Technology, Institute of Modern Optics, Nankai University, Tianjin, 300071, China.

^b Nanophotonics Research Center, Shenzhen University, Shenzhen, 518060, China.

^c Institute of Oncology, Tianjin Union Medical Centre, Tianjin, 300121, China.

These authors contribute equally to this work.

† Corresponding authors: Y. Yang, E-mail: yangyong@nankai.edu.cn, and X. Yuan, E-mail: xcyuan@szu.edu.cn.

Fig. S1 shows the simulated and experimentally generated ring-shaped POV spots with slightly increasing diameters, as well as the intensity profile curves across the spot centre in order to measure the spot diameter. The spot images (2000 pixel \times 2000 pixel) are obtained by a CCD camera (Hamamatsu C11440-22CU), with 6.5 μm \times 6.5 μm pixel sizes. By counting the pixels on the intensity profiles, we can calculate the different spot diameters respectively

Theory of graphene polarization property

As a two-dimensional material, graphene exhibits unique optoelectronic properties. The propagation of light through graphene is strongly influenced by its dynamic conductivity, which can be varied by an electric field, magnetic field, chemical doping, or by changing the gate bias voltage.³⁻⁵ The polarization mechanism can be theoretically analysed by applying Maxwell's equations under certain boundary conditions. Here, we give a detailed derivation on the graphene polarization property. Considering the infinitesimal thickness of monolayer graphene as compared with adjacent dielectrics, its thickness can be omitted while a dynamic conductivity σ_g is introduced at the interface.⁶⁻¹¹

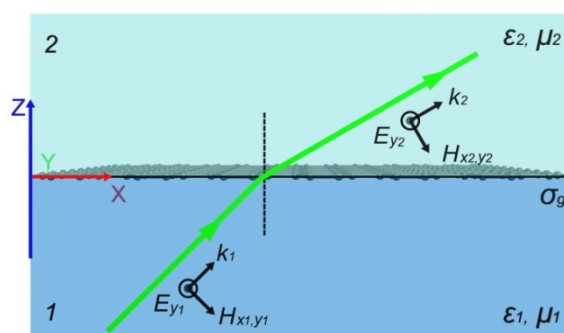


Fig. S2 Scheme of s-polarized wave at graphene interface.

The Maxwell's equations and the matter equations are:

$$\nabla \cdot \vec{D} = \rho \quad (\text{S1})$$

$$\nabla \cdot \vec{B} = 0 \quad (\text{S2})$$

$$\nabla \times \vec{E} = -\frac{\partial \vec{B}}{\partial t} \quad (\text{S3})$$

$$\nabla \times \vec{H} = \vec{j} + \frac{\partial \vec{D}}{\partial t} \quad (\text{S4})$$

$$\vec{j} = \sigma \vec{E} \quad (S5)$$

$$\vec{D} = \varepsilon \vec{E} \quad (S6)$$

$$\vec{B} = \mu \vec{H} \quad (S7)$$

For *s*-polarized incident wave, E_y , H_x , and H_z need to be considered, as shown in Fig. S2. Electrical and magnetic distributions can be defined as:

$$\vec{E}_y(r,t) = E_y e^{-i\omega t} \quad (S8)$$

$$\vec{H}_x(r,t) = H_x e^{-i\omega t} \quad (S9)$$

$$\vec{H}_z(r,t) = H_z e^{-i\omega t} \quad (S10)$$

In Dielectric 1 ($z < 0$), E_y can be expressed as:

$$E_{y1} = A_1 e^{i\beta x} e^{k_{z1} z} \quad (S11)$$

Thus H_x and H_z can be obtained by applying Eq. S3:

$$H_{x1} = iA_1 \frac{1}{\omega \mu_0 \mu_1} k_{z1} e^{i\beta x} e^{k_{z1} z} \quad (S12)$$

$$H_{z1} = A_1 \frac{\beta}{\omega \mu_0 \mu_1} e^{i\beta x} e^{k_{z1} z} \quad (S13)$$

And in Dielectric 2 ($z > 0$):

$$E_{y2} = A_2 e^{i\beta x} e^{-k_{z2} z} \quad (S14)$$

$$H_{x2} = -iA_2 \frac{1}{\omega \mu_0 \mu_2} k_{z2} e^{i\beta x} e^{-k_{z2} z} \quad (S15)$$

$$H_{z2} = A_2 \frac{\beta}{\omega \mu_0 \mu_2} e^{i\beta x} e^{-k_{z2} z} \quad (S16)$$

In the upper equations, β represents the propagation constant along *x*-axis, $k_{z1(2)}$ denotes the wave vector component along longitudinal direction in Dielectric 1(2), μ_0 is the vacuum permeability and $A_{\#}$ is an amplitude factor. For nonmagnetic materials, the relative permeability $\mu_{\#}$ is taken as 1. Applying boundary conditions $E_{y2} - E_{y1} = 0$ and $H_{x2} - H_{x1} = \sigma_g E_{y1}$ with conductivity σ_g introduced by graphene at interface $z = 0$, we obtain:

$$k_{z1} + k_{z2} = i\omega \mu_0 \sigma_g \quad (S17)$$

For $\vec{E}_y(r,t) = E_y e^{-i\omega t}$, the wave equation $\nabla^2 \vec{E} + \frac{\omega^2}{c^2} \varepsilon_r \vec{E} = 0$ can be written as:

$$\frac{\partial^2 E_y}{\partial z^2} + \left[\frac{\omega^2}{c^2} \varepsilon_r - \beta^2 \right] E_y = 0 \quad (S18)$$

Combine Eq. S11, Eq. S14 with Eq. S18, we can get:

$$k_{z\#}^2 = \beta^2 - \frac{\omega^2}{c^2} \varepsilon_{\#} \quad (S19)$$

Finally the dispersion equation for *s*-polarization mode can be described as:

$$\sqrt{\beta^2 - \frac{\omega^2}{c^2} \varepsilon_1} + \sqrt{\beta^2 - \frac{\omega^2}{c^2} \varepsilon_2} = i\omega \mu_0 \sigma_g \quad (S20)$$

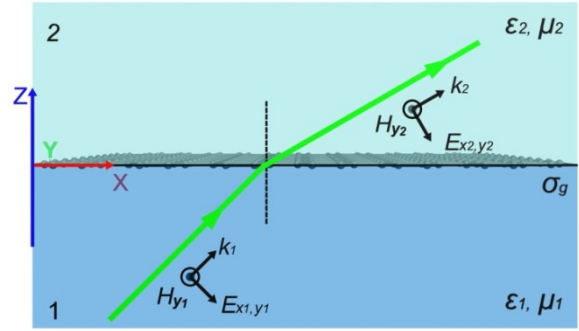


Fig. S3 Scheme of *p*-polarized wave at graphene interface.

Similarly, for *p*-polarized incident wave, H_y , E_x , and E_z need to be considered, as shown in Fig. S3. The electrical and magnetic distributions are given as:

$$\vec{H}_y(r,t) = H_y e^{-i\omega t} \quad (S21)$$

$$\vec{E}_x(r,t) = E_x e^{-i\omega t} \quad (S22)$$

$$\vec{E}_z(r,t) = E_z e^{-i\omega t} \quad (S23)$$

In Dielectric 1 ($z < 0$), H_y can be expressed as:

$$H_{y1} = A_1 e^{i\beta x} e^{k_{z1} z} \quad (S24)$$

Thus E_x and E_z can be obtained by applying Eq. S4:

$$E_{x1} = -iA_1 \frac{1}{\omega \varepsilon_0 \varepsilon_1} k_{z1} e^{i\beta x} e^{k_{z1} z} \quad (S25)$$

$$E_{z1} = -A_1 \frac{\beta}{\omega \varepsilon_0 \varepsilon_1} e^{i\beta x} e^{k_{z1} z} \quad (S26)$$

And in Dielectric 2 ($z > 0$):

$$H_{y2} = A_2 e^{i\beta x} e^{-k_{z2} z} \quad (S27)$$

$$E_{x2} = iA_2 \frac{1}{\omega \varepsilon_0 \varepsilon_2} k_{z2} e^{i\beta x} e^{-k_{z2} z} \quad (S28)$$

$$E_{z2} = -A_2 \frac{\beta}{\omega \varepsilon_0 \varepsilon_2} e^{i\beta x} e^{-k_{z2} z} \quad (S29)$$

Here, ε_0 is the vacuum permittivity, $\varepsilon_{\#}$ is the relative permittivity in Dielectric 1(2). Applying boundary conditions $E_{x2} - E_{x1} = 0$ and $H_{y1} - H_{y2} = \sigma_g E_{x1}$ at interface $z = 0$, we obtain:

$$\frac{A_1 k_{z1}}{\varepsilon_1} = \frac{A_2 k_{z2}}{\varepsilon_2} \quad (S30)$$

$$A_1 - A_2 = \frac{i k_{z2} \sigma_g A_2}{\omega \varepsilon_0 \varepsilon_2} \quad (S31)$$

Thus,

$$\frac{\varepsilon_1}{k_1} + \frac{\varepsilon_2}{k_2} = -\frac{i \sigma_g}{\omega \varepsilon_0} \quad (S32)$$

For $\vec{H}_y(r,t) = H_y e^{-i\omega t}$, the wave equation $\nabla^2 \vec{H} + \frac{\omega^2}{c^2} \varepsilon_r \vec{H} = 0$ is written as:

$$\frac{\partial^2 H_y}{\partial z^2} + \left(\frac{\omega^2}{c^2} \varepsilon_r - \beta^2 \right) H_y = 0 \quad (S33)$$

Combine Eq. S24, Eq. S27 with Eq. S33, we obtain:

$$k_{z\#}^2 = \beta^2 - \frac{\omega^2}{c^2} \varepsilon_{\#} \quad (S34)$$

Consequently, the dispersion equation for *p*-polarization mode can be described as:

$$\frac{\varepsilon_1}{\sqrt{\beta^2 - \frac{\omega^2}{c^2}\varepsilon_1}} + \frac{\varepsilon_2}{\sqrt{\beta^2 - \frac{\omega^2}{c^2}\varepsilon_2}} = -\frac{i}{\omega\varepsilon_0}\sigma_g \quad (\text{S35})$$

In summary, Eq. S20 and Eq. S35 are the dispersion equations for s -polarization (TE) and p -polarization (TM) modes respectively. Graphene could support the transmission of s -polarized (p -polarized) incident light when the imaginary part of the dynamic conductivity σ_g is negative (positive).

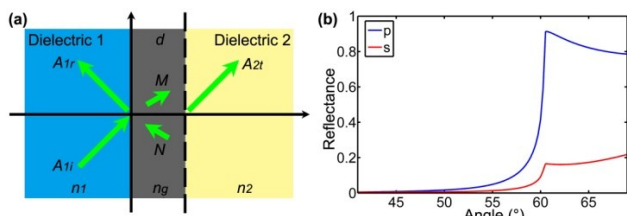


Fig. S4 (a) Dielectric-graphene-dielectric three-layer-film model. (b) Reflectance of p - and s -polarizations via incident angle.

Another method to explain the polarization-sensitive absorption property of graphene is to consider graphene as a medium with specific complex refractive index (n_g) and thickness (d).¹²⁻¹⁵ A three-layer-dielectric model, where graphene is sandwiched between a high refractive index medium (n_1) and a low refractive index medium (n_2), is shown in Fig. S4(a). The reflectance of p -polarized incident light or s -polarized incident light can be calculated by transfer matrix method under the framework of Fresnel reflection and refraction formulas.^{16,17} Fig. S4(b) gives the reflectance of p - and s -polarization varied with the incident angle respectively, with $n_1 = 1.53$, $n_2 = 1.33$, $n_g = 2.67 + 1.33i$ and $d = 3.8 \text{ nm}$. There is an obvious reflectance difference for graphene between p - and s -polarization. The reflectance difference will differ as the ambient refractive index changes, which is the theoretical basis of the graphene-based sensing and imaging method.

Transformation between Scalar and Vector Polarizations Using Two Vortex-Wave Plates

The fast axis direction of each point on the vortex wave plate is half the azimuth angle deflection from its azimuth angle direction, as shown in Fig. S5(a). It can be depicted by a Jones matrix as:

$$\begin{bmatrix} \cos\theta & \sin\theta \\ \sin\theta & -\cos\theta \end{bmatrix} \quad (\text{S36})$$

Here, θ is the azimuth angle. Horizontally linear polarization is converted into radial polarization after passing through the vortex wave plate:

$$\begin{bmatrix} \cos\theta & \sin\theta \\ \sin\theta & -\cos\theta \end{bmatrix} \begin{bmatrix} 1 \\ 0 \end{bmatrix} = \begin{bmatrix} \cos\theta \\ \sin\theta \end{bmatrix} \quad (\text{S37})$$

While for vertically linear polarization, it becomes azimuthal polarization:

$$\begin{bmatrix} \cos\theta & \sin\theta \\ \sin\theta & -\cos\theta \end{bmatrix} \begin{bmatrix} 0 \\ 1 \end{bmatrix} = \begin{bmatrix} \sin\theta \\ -\cos\theta \end{bmatrix} \quad (\text{S38})$$

Arbitrarily linear polarization with azimuth angle α becomes a generalized cylindrical vector beam with the polarization of each point rotated clockwise by angle α from its radial direction:

$$\begin{bmatrix} \cos\theta & \sin\theta \\ \sin\theta & -\cos\theta \end{bmatrix} \begin{bmatrix} \cos\alpha \\ \sin\alpha \end{bmatrix} = \begin{bmatrix} \cos\theta\cos(\theta-\alpha) \\ \sin\theta\cos(\theta-\alpha) \end{bmatrix} \quad (\text{S39})$$

The proportion of radial and azimuthal components is determined by the direction of the original linear polarization, as shown in Fig. S5(b)-S5(c).

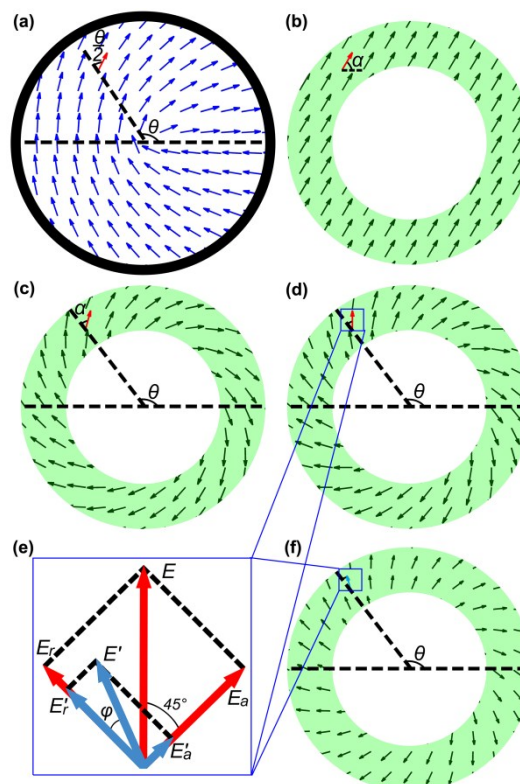


Fig. S5 Analysis of the vortex wave plate and cylindrical vortex beams using the Jones matrix. (a) Fast axis orientation of a vortex wave plate. (b) Sketch of a linearly polarized POV beam, with angle α between its polarization direction and horizontal direction. (c) Sketch of a α -GCVP POV beam. (d) Sketch of the incident 45-GCVP POV beam before focusing. (e) Polarization variations between incident and reflected beams. (f) Sketch of the reflected φ -GCVP POV beam from the objective, its radial and azimuthal components have been changed owing to different absorptions by graphene.

We find that the vector beam will be demodulated back to its original linear polarization by adding another vortex wave plate after the beam:

$$\begin{bmatrix} \cos\theta & \sin\theta \\ \sin\theta & -\cos\theta \end{bmatrix} \begin{bmatrix} \cos\theta & \sin\theta \\ \sin\theta & -\cos\theta \end{bmatrix} \begin{bmatrix} \cos\alpha \\ \sin\alpha \end{bmatrix} = \begin{bmatrix} \cos\alpha \\ \sin\alpha \end{bmatrix} \quad (\text{S40})$$

As the focusing spot of the 45-GCVP beam is mixed with p - and s -polarizations, and graphene exhibits larger absorption of s -polarized light as compared with p -polarized light, the polarization direction of the reflected beam will be different from the incident beam. We assume R_p and R_s as the reflectivity coefficients of graphene to p - and s -polarizations respectively. R_p is much larger than R_s , and both are sensitive to slight refractive index variations of the sample on top of graphene. For the incident beam, as shown in Fig. S5(e), the radial component of each point is equal to its azimuthal component:

$$E_r = E_a = \frac{\sqrt{2}}{2}E \quad (\text{S41})$$

Where E represents the electric field intensity of an arbitrary point on the incident beam, and E_r and E_a are the radial and azimuthal components of the point. The radial and azimuthal components of the incident beam contribute to p - and s -polarizations on the focusing spot, respectively. The components of the reflected beam will be different from the incident beam

owing to the absorption difference of graphene, as shown in Fig. S5(f):

$$E'_r = R_p E_r = \frac{\sqrt{2}}{2} R_p E \quad (\text{S42})$$

$$E'_a = R_s E_a = \frac{\sqrt{2}}{2} R_s E \quad (\text{S43})$$

$$E' = \sqrt{E_r'^2 + E_a'^2} = \sqrt{\frac{R_p^2 + R_s^2}{2}} E \quad (\text{S44})$$

$$\varphi = \arctan\left(\frac{E'_a}{E'_r}\right) = \arctan\left(\frac{R_s}{R_p}\right) \quad (\text{S45})$$

Where E'_r and E'_a denote the radial and azimuthal field intensity components of the point on reflected beam, and φ is the angle between its electric field direction and radial direction at the point. As a result, the reflected beam becomes a φ -GCVP beam. According to Eq. S40, the beam returns to linear polarization with azimuth angle φ after passing through a vortex wave plate. The azimuth angle φ is determined by the reflectivity difference to p - and s -polarizations. The beam is split by a polarizing beam splitter into two beams, representing residual p - and s -polarization intensities. Additionally, a balanced detector will record the signal differences as the refractive index of the sample changes.

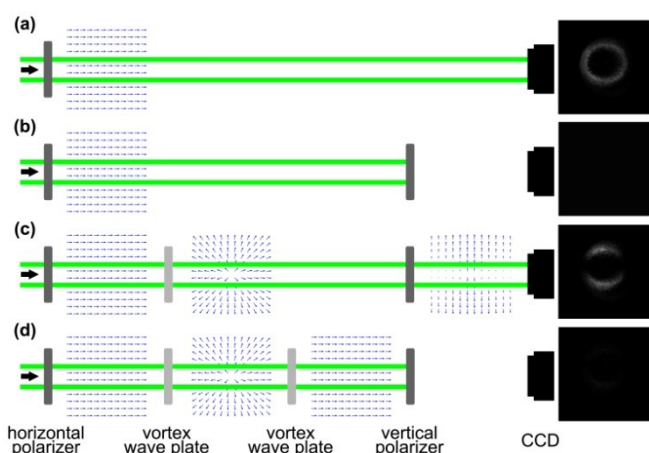


Fig. S6 (a) A horizontal polarizer transforms the beam into linear polarization. (b) A vertical polarizer stops the horizontally polarized beam from entering the CCD. (c) A vortex-wave plate inserted between the polarizers will transform the incident beam into radial polarization, only the vertical components of the beam can reach the CCD camera after passing through the vertical polarizer. (d) A second vortex-wave plate added after the first one will transform the radially polarized beam back into original linear polarization.

In experiments, a vortex-wave plate is employed to transform a linearly polarized beam into cylindrical vector beam, and a second one is to demodulate the cylindrical vector beam back to its original linear polarization. The theory has been demonstrated in the main text, here we experimentally verify this property, as shown in Fig. S6. In Procedure (a), the beam is modulated to horizontal linear polarization by a horizontal polarizer, and the spot is recorded by a CCD camera; In Procedure (b), a vertical polarizer is added in the path, then the horizontally polarized beam is stopped, there is no light incident into the CCD camera; In Procedure (c), a vortex-wave plate is inserted between the two polarizers, the horizontally polarized beam is first transformed into radial polarization, and then only the vertical components could pass through the vertical polarizer, the spot is shown in the

CCD image; In Procedure (d), a second vortex-wave plate is added after the first vortex-wave plate in the path. The radially polarized beam is demodulated back to horizontal polarization, and again no lights could reach the CCD camera.

Spatial Resolution Measurement

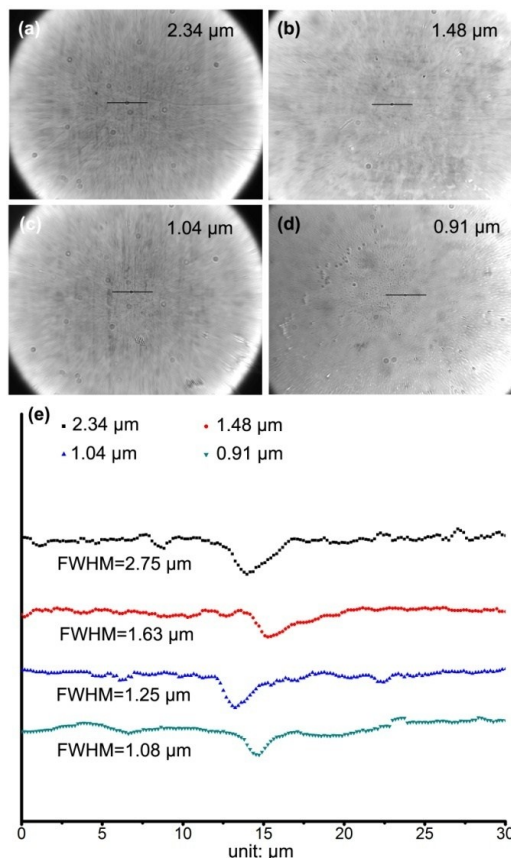


Fig. S7 CCD images of (a) 2.34 μm , (b) 1.48 μm , (c) 1.04 μm , and (d) 0.91 μm microspheres respectively. (e) One group of measured intensity curves of the microspheres with different mean diameters.

Experimentally, polystyrene (PS) microspheres of different diameters are employed to calibrate the experimental spatial resolution, as shown in Fig. S7. Fig. S7(a)-(d) show the CCD images of microspheres with different given mean diameters respectively. The black solid lines in the images indicate the scanning path. Fig. S7(e) gives one group of the measured intensity curves across the microsphere centres. As the diameters decrease from 2.34 μm to 0.91 μm , the measurement shows good signal-noise ratio and high stability. When the diameter further decreases to smaller one, the detected signal intensity becomes too weak to analyse the signal curve and obtain accurate measurement values. After several groups of repeated measurements, the mean FWHM for 0.91 μm microsphere is 1.07 μm , which is taken as the experimental spatial resolution of the system.

Growth, Transferring, and Characterization of Graphene

The graphene samples on the 0.17-mm-thick glass cover slip substrate are customized from Nanjing XFNANO Materials Tech Co., Ltd, which is first prepared by chemical vapor

deposition on copper substrate, and is then transferred onto the surface of the copper cover slip via a heat-sensitive adhesive transfer method.¹⁸⁻²⁰ The growth and transferring processes mainly include the following steps and are illustrated in Fig. S8.

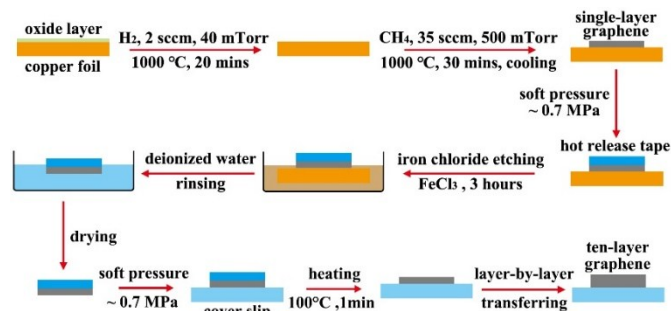


Fig. S8 Growth and transferring process for 10-layer CVD graphene on glass cover slip substrate.

1. Single-layer graphene is prepared by chemical vapor deposition method on the transition metal substrate.

(a) The copper substrate is processed under hydrogen atmosphere at $1000\text{ }^\circ\text{C}$ for around 20 minutes to remove the surface oxide layer and increase catalytic activity. The flow rate and pressure of hydrogen are 2 sccm and 40 mTorr, respectively.

(b) While keeping the pressure and flow rate of hydrogen steady at $1000\text{ }^\circ\text{C}$, methane with 35 sccm and 500 mTorr is introduced for 30 minutes.

(c) While keeping the pressure and flow rate of hydrogen and methane steady, the substrate is cooled down to room temperature with a $50\text{ }^\circ\text{C}/\text{min}$ cooling rate.

2. Single-layer graphene is transferred from the copper substrate to a 0.17-mm-thick glass cover slip through a heat-sensitive adhesive transfer method.

(a) A hot release tape is attached to the graphene layer with 0.7 MPa pressure.

(b) The sample is etched in ferric chloride solution for 3 hours and rinsed with deionized water repeatedly to remove the copper substrate.

(c) After drying, the sample is attached to the glass cover slip surface with 0.7 MPa pressure, and then heated at $100\text{ }^\circ\text{C}$ for 1 minute to separate the graphene on cover slip substrate from the hot release tape.

3. Single-layer graphene is repeatedly superposed on the glass cover slip layer by layer to obtain the final 10-layer graphene for experimental use.

Fig. S9(a) shows the photograph of a graphene sample. After the graphene samples are fabricated, Raman spectra at two arbitrary areas and thickness characterization by atomic force microscopy (AFM) are provided, as shown in Fig. S9(b)-(d). The AFM measurement indicates a thickness of around 3.8 nm for the 10-layer graphene.

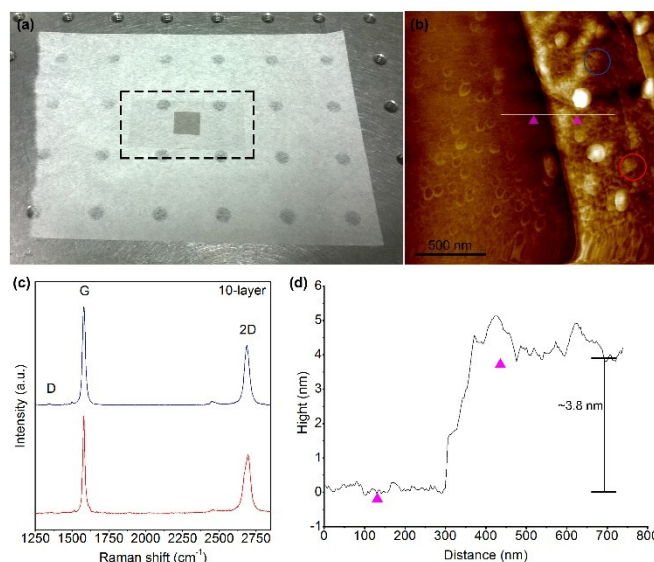


Fig. S9 Characterization of a 10-layer graphene sample on glass cover slip substrate by Raman spectra and AFM. (a) Photograph of the graphene sample, the darker area in the centre is graphene. (b) AFM image of the graphene sample. (c) Raman spectra at two different positions as marked in Fig. S9(a). (d) Thickness measurement of the graphene film by AFM.

Preparation for Graphene Sensor Chip and Cell Culture

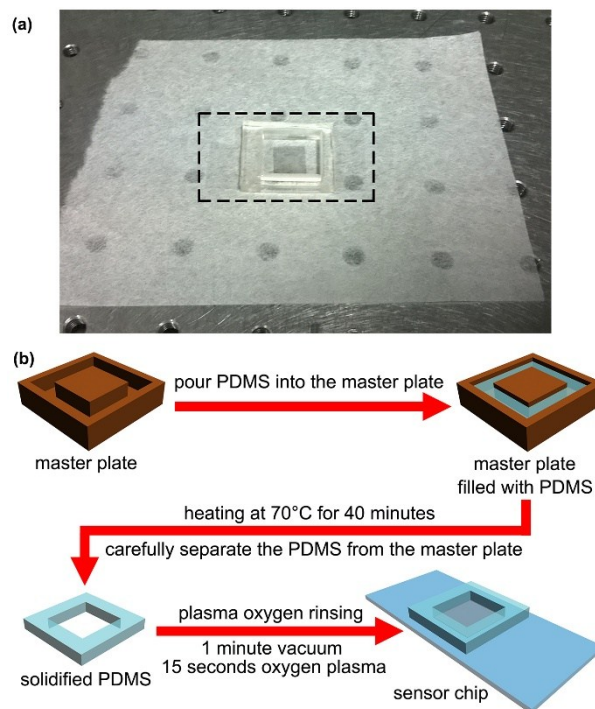


Fig. S10 Preparation for graphene sensor chip (a) Photograph and (b) fabrication process of a cell culture dish.

A cell culture dish is fabricated around graphene using polydimethylsiloxane (PDMS), which is highly biocompatible. As illustrated in Fig. S10(b), the silicone elastomer base and curing agent are proportionally mixed (10:1) and slowly poured into a specific master plate. After heating at $70\text{ }^\circ\text{C}$ for 40 minutes, the PDMS mixture becomes solidified and is carefully separated

from the master plate. Then the hollow PDMS model is placed on the graphene-coated cover slip, and processed in the oxygen plasma rinsing machine for 1 minute vacuum and 15 seconds oxygen plasma processing. Finally the PDMS model and the cover slip bond together tightly and the graphene sensor chip is produced, which is used to culture cells, as shown in Fig. S8(b).

Then sensor chip is treated with 0.02 mg/mL poly-L-lysine for 16 hours and washed twice with Hank's balanced salt solution (137.93 mM NaCl, 5.33 mM KCl, 4.17 mM NaHCO₃, 0.441 mM KH₂PO₄, 0.338 mM Na₂HPO₄, and 5.56 mM D-glucose). Cells are trypsinized and seeded on the graphene surface of the sensor chip. For adhering cells onto the surface, the sensor chip is filled with culture medium and maintained at 37 °C in a 5% CO₂ incubator for 8 hours. Finally, the cells are completely adhered to the graphene surface.²¹

Comparison between Cell Refractive Index Distribution and Fluorescence Image

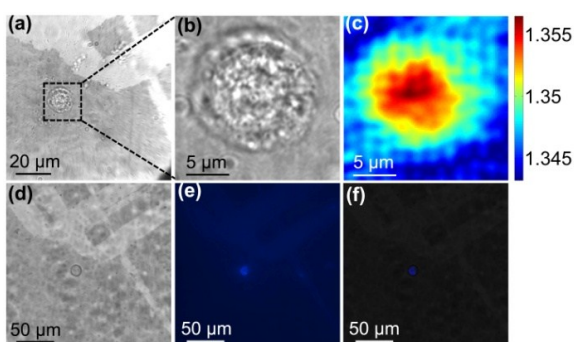


Fig. S11 (a) Bright field image of a human colonic cancer cell obtained in the proposed experimental setup, with a 100× microscope objective. (b) Enlarged bright field image of the cell. (c) Refractive index mapping image of the cell with 20 μm × 20 μm scanning range and 0.2 μm scanning step. (d) Bright field image of the same cell under fluorescence microscope with a 60× microscope objective. (e) Fluorescent image of the cell nucleus. (f) Superposition image of the bright field image and fluorescent image.

A comparison between cell refractive index distribution and fluorescence image of the same cell is conducted in experiment. The results are given in Fig. S11. Fig. S11(a) shows the bright field image of a living human colonic cancer cell obtained with the 100× microscope objective in the proposed optical configuration. The cell refractive index mapping image is shown in Fig. S11(c) with 20 μm × 20 μm scanning range and 0.2 μm scanning step. After the refractive index mapping process, the cell is treated with DAPI (4', 6-diamidino-2-phenylindole), which is used for fluorescent nuclear staining. Then the same cell is observed under a commercial fluorescence microscope (Nikon, Eclipse Ti-S) with a 60× microscope objective. Fig. S11(d) is the bright field image of the cell under the fluorescence microscope, and Fig. S11(e) is the fluorescent image of the cell nucleus, which is obtained by switching the filter of the fluorescence microscope without moving the samples. So the superposition of bright field image [Fig. S11(d)] and fluorescent image [Fig. S11(e)] could indicate the nucleus position inside the cell, as shown in Fig. S11(f). At the nuclear area, it shows relatively higher refractive index for colonic cancer cells, which may be due to the presence of dense chromatin in nucleus.^{22,23} The refractive index imaging method provides a label-free and non-invasive means for living cell microscopy. It should be noted that refractive index is non-specific to cell organelles. It will be of great interest in cell refractive index-related

researches, such as the monitoring of cell growth, evolution and apoptosis at different stages, observation of cell mitosis, cell response to drugs and other external stimulus, normal and abnormal cell cycle detection and analysis, etc. We believe that the combination of refractive index imaging and biomarker techniques will make researchers gain deeper insight into cell mechanisms.

References

- J. García-García, C. Rickenstorff-Parrao, R. Ramos-García, V. Arrizón, and A. S. Ostrovsky, *Opt. Lett.*, 2014, **39**, 5305-5308.
- P. Vaity and L. Rusch, *Opt. Lett.*, 2015, **40**, 597-600.
- Q. L. Bao and K. P. Loh, *ACS Nano*, 2012, **6**, 3677-3694.
- X. R. Wang, X. L. Li, L. Zhang, Y. Yoon, P. K. Weber, H. L. Wang, J. Guo, and H. J. Dai, *Science*, 2009, **324**, 768-771.
- J. T. Kim and C. G. Choi, *Opt. Express*, 2012, **20**, 3556-3562.
- Q. L. Bao, H. Zhang, B. Wang, Z. H. Ni, C. H. Y. X. Lim, Y. Wang, D. Y. Tang, and K. P. Loh, *Nat. Photon.*, 2011, **5**, 411-415.
- S. A. Mikhailov and K. Ziegler, *Phys. Rev. Lett.*, 2007, **99**, 016803.
- M. Jablan, H. Buljan, and M. Soljagic, *Phys. Rev. B.*, 2009, **80**, 196-206.
- T. Stauber, N. M. R. Peres, and A. K. Geim, *Phys. Rev. B.*, 2008, **78**, 085432.
- G. W. Hanson, *J. Appl. Phys.*, 2008, **103**, 064302.
- X. Y. He and R. Li, *IEEE J. Quantum Electron.*, 2014, **20**, 4600106.
- X. F. Wang, Y. P. Chen, and D. D. Nolte, *Opt. Express*, 2008, **16**, 22105-22112.
- M. Bruna and S. Borini, *Appl. Phys. Lett.*, 2009, **94**, 031901.
- J. W. Weber, V. E. Calado, and M. C. M. van de Sanden, *Appl. Phys. Lett.*, 2010, **97**, 091904.
- X. F. Wang, M. Zhao, and D. D. Nolte, *Appl. Phys. Lett.*, 2009, **95**, 081102.
- F. Xing, G. X. Meng, Q. Zhang, L. T. Pan, P. Wang, Z. B. Liu, W. S. Jiang, Y. S. Chen, and J. G. Tian, *Nano Lett.*, 2014, **14**, 3563-3569.
- Q. Ye, J. Wang, Z. B. Liu, Z. C. Deng, X. T. Kong, F. Xing, X. D. Chen, W. Y. Zhou, C. P. Zhang, and J. G. Tian, *Appl. Phys. Lett.*, 2013, **102**, 021912.
- S. Bae, H. Kim, Y. Lee, X. F. Xu, J. S. Park, Y. Zheng, J. Balakrishnan, T. Lei, H. R. Kim, Y. I. Song, Y. J. Kim, K. S. Kim, B. Ozyilmaz, J. H. Ahn, B. H. Hong, and S. Iijima, *Nat. Nanotech.*, 2010, **5**, 574-578.
- C. Mattevi, H. Kim, and M. Chhowalla, *J. Mater. Chem.*, 2011, **21**, 3324-3334.
- J. W. Suk, A. Kitt, C. W. Magnuson, Y. F. Hao, S. Ahmed, J. An, A. K. Swan, B. B. Goldberg, and R. S. Ruoff, *ACS Nano*, 2011, **5**, 6916-6924.
- Y. J. Wang, C. L. Zhang, Y. Q. Zhang, H. Fang, C. J. Min, S. W. Zhu, and X. C. Yuan, *Sens. Actuators B*, 2015, **209**, 313-322.
- R. S. Gurjar, V. Backman, L. T. Perelman, I. Georgakoudi, K. Badizadegan, I. Itzkan, R. R. Dasari, and M. S. Feld, *Nat. Med.*, 2001, **7**, 1245-1248.
- V. Backman, M. B. Wallace, L. T. Perelman, J. T. Arendt, R. Gurjar, M. G. Müller, Q. Zhang, G. Zonios, E. Kline, J. M. McGillican, S. Shapshay, T. Valdez, K. Badizadegan, J. M. Crawford, M. Fitzmaurice, S. Kabani, H. S. Levin, M. Seiler, R. R. Dasari, I. Itzkan, J. Van Dam, and M. S. Feld, *Nature*, 2000, **406**, 35-36.